Research Article Vol. 31, No. 14 / 3 Jul 2023 / Optics Express 23551
Optics EXPRESS

Non-collinear generation of ultra-broadband parametric fluorescence photon pairs using chirped quasi-phase matching slab waveguides

Bo Cao,[1] Kyohei Hayama,[1] Shun Suezawa,[1] Mamoru Hisamitsu,[2] Katsuhiko Tokuda,[2] Sunao Kurimura,[3] Ryo Okamoto,[1,4] and Shigeki Takeuchi[1,*]

[1]Department of Electronic Science and Engineering, Kyoto University, Kyotodaigakukatsura, Nishikyo-ku, Kyoto 615-8510, Japan
[2]Shimadzu Corporation, 3-9-4 Hikaridai, Seika-cho, Soraku-gun, Kyoto 619-0237, Japan
[3]National Institute for Materials Science (NIMS), 1-1 Namiki, Tsukuba, Ibaraki 305-0044, Japan
[4]Japan Science and Technology Agency, PRESTO, Gobancho, Chiyoda-ku, Tokyo 102-0076, Japan
*takeuchi@kuee.kyoto-u.ac.jp

Abstract: Many optical quantum applications rely on broadband frequency correlated photon pair sources. We previously reported a scheme for collinear emission of high-efficiency and ultra-broadband photon pairs using chirped quasi-phase matching (QPM) periodically poled stoichiometric lithium tantalate (PPSLT) ridge waveguides. However, collinearly emitted photon pairs cannot be directly adopted for applications that are based on two-photon interference, such as quantum optical coherence tomography (QOCT). In this work, we developed a chirped QPM device with a slab waveguide structure. This device was designed to produce spatially separable (photon pair non-collinear emission) parametric fluorescence photon pairs with an ultra-broadband bandwidth in an extremely efficient manner. Using a non-chirped QPM slab waveguide, we observed a photon pair spectrum with a full-width-at-half-maximum (FWHM) bandwidth of 26 nm. When using a 3% chirped QPM slab waveguide, the FWHM bandwidth of the spectrum increased to 190 nm, and the base-to-base width is 308 nm. We also confirmed a generation efficiency of 2.4×10^6 pairs/(μW·s) using the non-chirped device, and a efficiency of 8×10^5 pairs/(μW·s) using the 3% chirped device under non-collinear emission conditions after single-mode fiber coupling. This is, to the best of our knowledge, the first report of frequency correlated photon pairs generation using slab waveguide device as a source. In addition, using slab waveguides as photon pair sources, we performed two-photon interference experiments with the non-chirped device and obtained a Hong–Ou–Mandel (HOM) dip with a FWHM of 7.7 μm and visibility of 98%. When using the 3% chirped device as photon pair source, the HOM measurement gave a 2 μm FWHM dip and 74% visibility.

1. Introduction

Broadband parametric fluorescence photon pairs play an essential role in many quantum optical applications, including quantum information processing [1–3], quantum communication [4,5], and quantum sensing employing frequency correlated photons, which are being intensively developed, including for instance spectroscopy using frequency entangled photon pairs [6], quantum infrared spectroscopy [7–9], and quantum optical coherence tomography with dispersion tolerance [10–13]. In addition, broadband frequency correlated photon pairs are being used for efficiency enhancement of two-photon absorption [14,15].

Numerous methods to generate broadband frequency correlated photon pairs have been documented, including generation of frequency correlated photon pairs with a spectral bandwidth of 80 nm using a thin $\chi^{(2)}$ bulk crystal [10,16] and broadband parametric fluorescence photon

#488978 https://doi.org/10.1364/OE.488978
Journal © 2023 Received 2 Mar 2023; revised 19 May 2023; accepted 20 May 2023; published 29 Jun 2023

Optics EXPRESS

pair generation with a spectral bandwidth of 160 nm using the superposition of phase matching of spontaneous parametric down conversion (SPDC) processes in two beta barium borate (BBO) crystals [17]. A scheme that simultaneously uses two SPDC processes in a single QPM device is being developed to generate broadband visible-infrared frequency correlated photon pairs [18]. There are reports on the generation of bi-photons with bandwidths exceeding 100 THz via utilizing the group velocity matching in $KTiOPO_4$ (KTP) based devices [19,20]. In addition, using nonlinear fibers, the bi-photons have been generated with a bandwidth of more than 55 THz [21]. Also of note is a method of observing large variable wavelength ranges of photons by tuning the angle of a $\chi^{(2)}$ nonlinear crystal [22]. Recently, in addition to SPDC-based devices, photon pairs with ultra-broadband frequency correlation and comb-like spectra have been generated using silicon-based ring resonator cavities [23,24].

To the best of our knowledge, frequency correlated photon pairs with the largest spectral bandwidth in frequency (194 THz) are generated using chirped QPM devices [25]. In contrast to commonly used non-chirped QPM devices that have a poling period with a fixed length throughout the device, chirped QPM devices have multiple poling periods with varying lengths, which leads to the occurrence of multiple SPDC processes and the emission of photons with various colors. Since this scheme was proposed [26,27], the development of devices based on chirped QPM has rapidly picked up, and many studies have been published on the generation of ultra-broadband (bandwidth >100 nm) frequency correlated photon pairs [25,28,29].

Recently, to improve the brightness of chirped QPM photon pair sources while maintaining ultra-broadband spectral bandwidth generation, a scheme using chirped QPM periodically poled stoichiometric lithium tantalate (PPSLT) with a ridge waveguide structure [30] was developed. Using such a device, the authors managed to observe 320 nm ultra-broadband photon pair generation with a hundred times higher generation efficiency compared to bulk chirped QPM devices.

Despite the promising results obtained, chirped QPM ridge waveguides have an issue compared to chirped QPM bulk crystals in that when employing ridge waveguide devices as photon pair sources, the frequency correlated photon pairs are collinearly emitted into the same spatial mode, i.e., the guided mode of the ridge waveguide. A scheme using time-reversed Hong-Ou-Mandel (HOM) interference has been proposed and demonstrated to separate collinearly emitted two frequency degenerated photons that also share the same polarization [31,32]. However, using this scheme, the efficiency of photon pairs separation is dependent on the performance of quantum interference, which is technically difficult and will be more challenging when photons have a larger bandwidth. This makes it difficult to adopt ridge waveguide-based photon pair sources directly into existing two-photon interference applications. That is to say, conventional chirped QPM bulk crystals can emit photon pairs into different spatial modes but are not bright enough to be used as photon pair sources, whereas chirped QPM ridge waveguide devices are very bright but only emit photon pairs in the same spatial mode. In this work, we propose a chirped QPM PPSLT device that has a slab waveguide structure to serve as an ultra-bright and ultra-broadband parametric fluorescence photon pair source that emits photons into separated spatial modes (non-collinear emission). To the best of our knowledge, this is the first report of frequency correlated photon pairs generation using slab waveguides as sources. In experiments, we observed a spectrum with a bandwidth of 26 nm using a non-chirped QPM slab waveguide, and a bandwidth of 308 nm (base-to-base width) using a 3% chirped QPM waveguide. We also have carried out experiments to assess the photon pair generation efficiency under non-collinear emission after single-mode fiber coupling. Using the non-chirped device, the generation efficiency is 2.4×10^6 pairs/(μW·s), while using the 3% chirped device it is 8×10^5 pairs/(μW·s). Additionally, we performed a two-photon interference experiment using slab waveguides as photon pair sources and obtained a Hong–Ou–Mandel (HOM) dip with a full width half maximum (FWHM) of

Optics EXPRESS

7.7 μm and a visibility of 98% using the non-chirped device, and a 2 μm FWHM dip and 74% visibility using the 3% chirped device.

This paper is organized as follows. In the section 2, we introduce our slab waveguides in detail, as well as the method for theoretically predicting SPDC spectra using non-chirp and chirped QPM devices. The section 3 presents a second harmonic generation (SHG) experiment and the results using a non-chirped slab waveguide. Then, under non-collinear emission phase-matching conditions, we carry out two experiments to evaluate photon pair generation. The experiments and results of measuring the photon spectra are shown in the subsection 4.1. The experiments and results of the evaluation of photon generation efficiency are described in subsection 4.2. Additionally, utilizing slab waveguides as photon pair sources, we perform a two-photon interference experiment. The experiment and its results are given in section 5.

2. Device

Figure 1(a) depicts a schematic view of our 20-mm-long QPM slab waveguide. Two resin cladding layers sandwich a Mg-doped SLT (Mg:SLT) layer with a thickness of ~ 3.1 μm that forms the slab waveguide core. The non-chirped QPM slab waveguide has a fixed poling period of 3.19 μm along the device. We also developed a chirped QPM slab waveguide with a chirp rate of $r = 3\%$. This chirped device is composed of 10 equal-length segments, each with a different poling-period length Λ_m. The length of the poling period Λ_m for the m-th segment is given by

$$\frac{1}{\Lambda_m} = \frac{1}{\Lambda_0}\left(1 - \frac{m-1}{1+r}\frac{r}{n-1}\right), \tag{1}$$

where $\Lambda_0 = 3.19$ μm is the minimum poling period of the chirped QPM device, $r = 3\%$ is the chirp rate, m denotes the m-th segment, and $n = 10$ is the total number of segments in this chirped QPM device. The phase matching function for a QPM device, as is well known, can be expressed as the Fourier transform of the nonlinearity spatial profile [33]

$$\Phi(\lambda_s, \lambda_i) \propto \int_0^L \chi^{(2)} \mathrm{Exp}\left(-i\Delta k(\lambda_s, \lambda_i)z\right) \mathrm{d}z, \tag{2}$$

where L is the length of the QPM device, $\chi^{(2)}$ is the 2nd order nonlinearity, λ_s and λ_i are the wavelengths of signal and idler photons, respectively, and Δk is the phase mismatch.

For a device with a poling-period spatial profile $\Lambda(z)$, the quasi-phase matching function is [25]:

$$\begin{aligned}\Delta k(\lambda, T, \theta) =& \beta_p(\lambda_p, T) - \beta_s(\lambda_s, T)\sqrt{1 - \left(\frac{\sin(\theta)}{n(\lambda_s, T)}\right)^2} \\ &- \beta_i(\lambda_i, T)\sqrt{1 - \left(\frac{\lambda_i}{\lambda_s}\right)^2\left(\frac{\sin(\theta)}{n(\lambda_i, T)}\right)^2} - \frac{2\pi}{\Lambda(z)},\end{aligned} \tag{3}$$

where λ_p, λ_s, and λ_i are the wavelengths of pump, signal, and idler photons, respectively, T is the device temperature, and θ is the SPDC light emission angle. The effective refractive index inside the slab waveguide is $n(\lambda)$, and the wave vectors for the pump, signal, and idler light are β_i (i = p, s, i). For a non-chirped device, $\Lambda(z)$ is constant throughout the device length L. In contrast, in a linearly chirped QPM device, $\Lambda(z)$ is a step function.

In the calculation of the effective refractive index of the slab waveguide, the cladding layers were assumed to have a constant refractive index of $n_{clad} = 1.5$, and the refractive index for the Mg-SLT core layer was calculated using the Sellmeier equation [34]. The effective refractive index for the fundamental mode in the slab waveguide was estimated using a finite-difference time-domain (FDTD) simulation (COMSOL). In the calculation of SPDC spectra using slab

Optics EXPRESS

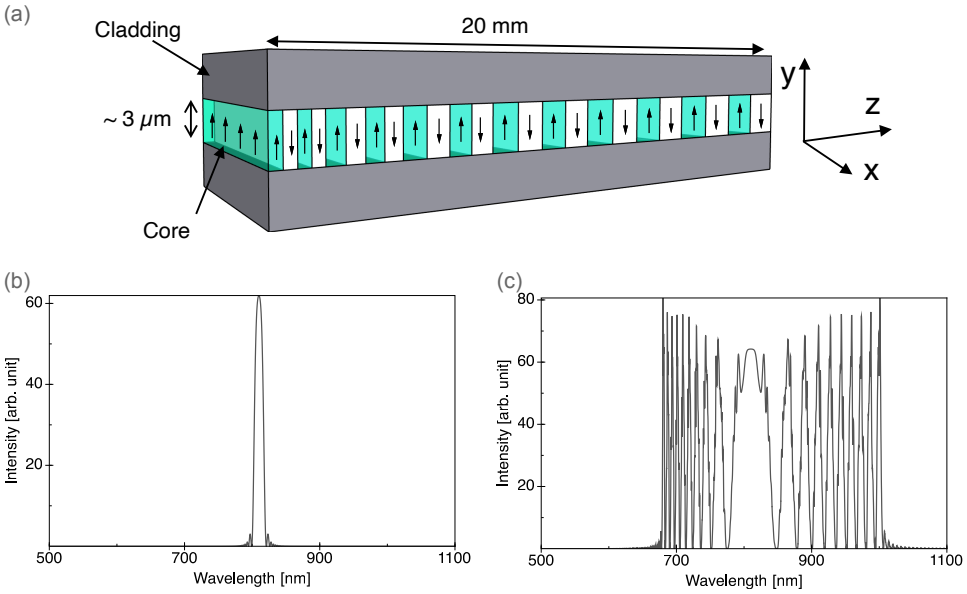

Fig. 1. (a) Schematic view of QPM PPSLT slab waveguide consisting of two cladding resin layers and a Mg-SLT layer with a height of 3.1 μm as the waveguide core. The domains with arrows represent the periodically poled structure. The length of this device is about 20 mm. (b) Theoretically calculated spectra with FWHM bandwidth of 11.3 nm. This spectrum was calculated assuming a non-chirped QPM slab waveguide under collinear emission conditions and pumped by 405 nm continuous wave (CW) light. (c) Predicted spectrum for 3% chirped QPM slab waveguide with ~ 330 nm FWHM bandwidth.

waveguides, we did not incorporate any slab waveguide properties other than the effective refractive index. The device's thermal expansion impact was also not included. We assumed a continuous wave (CW) pump with a wavelength of 405 nm, applied the effective refractive index to Eq. (3), and then calculated the spectra of parametric fluorescence generated under a collinear emission condition using a non-chirped QPM slab waveguide (Fig. 1(b)) and a 3% chirped waveguide (Fig. 1(c)). With a non-chirped device, the calculated spectrum has a sinc-like shape with a FWHM bandwidth of 13.4 nm. We also obtained an extended spectrum with a FWHM width of 329 nm using a 3% chirped waveguide. The comb-like spectrum of the chirped device is caused by interference of numerous phase matching functions with discrete periodically poled lengths. A flatter spectrum can be obtained by increasing the number of segments in the chirped QPM device [11,25].

3. Second harmonic generation using non-chirped QPM slab waveguide

To test this slab waveguide, we carried out a second harmonic generation (SHG) measurement using a non-chirped QPM slab waveguide. In this experiment, we use 810 nm continuous wave (CW) light (Coherent, MBR110) as pump light. For coupling the pump beam into the slab waveguide, a pair of cylindrical lenses with focal lengths of 80 mm and 3.9 mm are used to condense the pump beam in the horizontal and vertical directions, respectively (Fig. 2(a)). The coupling efficiency of 810 nm pump light from air to waveguide is approximately 20%. During this measurement, the device temperature is kept at 59.2 °C. The upconverted light is measured by a power meter (Thorlabs, S130C) after eliminating the pump light using a shortpass filter.

Optics EXPRESS

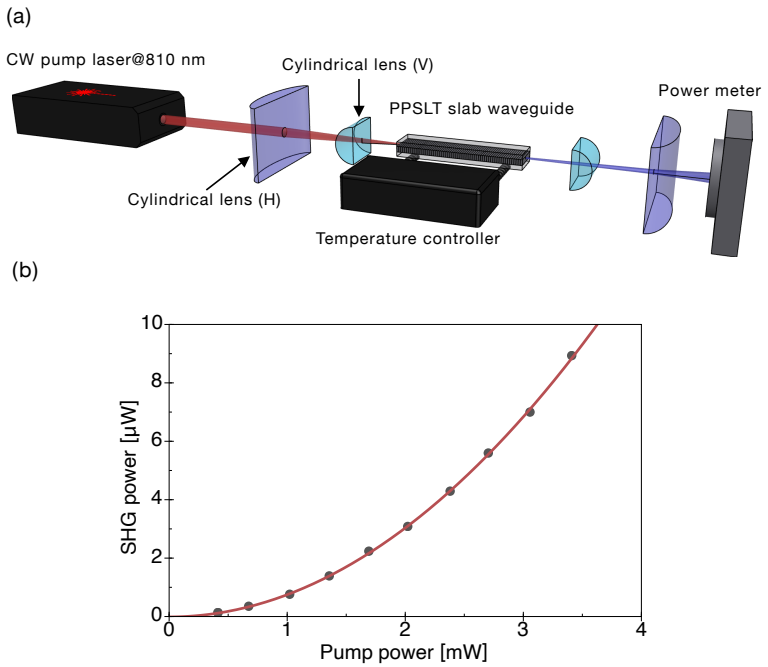

Fig. 2. (a) Experimental setup for SHG measurement. The 810 nm pump light beam is condensed horizontally by an f = 80 mm cylindrical lens and vertically by an f = 3.9 mm lens. The device temperature is set to 59.2 °C. The upconverted light is measured by a power meter. (b) Measured upconverted light power as function of pump light power.

Figure 2(b) shows the results for the measured upconverted light power $I_{2\omega}$ while altering the pump power I_{ω}. The red solid curve in Fig. 2 is the fitting result for $I_{2\omega} = \eta I_{\omega}^2$, where $\eta = 76\%$ /W is the normalized conversion efficiency. This result is about 7 times smaller than what we have obtained with a ridge waveguide device [30], as the slab waveguide only confines the pump beam in one dimension.

4. Non-collinear emission of photon pairs using slab waveguides

In contrast to the commonly used ridge waveguides, slab waveguide devices can be used for non-collinear photon pair emission in addition to collinear emission. This is an essential feature for applications like QOCT. We use the setup shown in Fig. 3(a) to experimentally observe the non-collinear emission of parametric light. In this experiment, a 405 nm CW laser (Coherent, MBR110, and MBD200) is used as the pump light, and the device temperature is controlled by a temperature controller (Cell system, TDB1700) with an accuracy of ± 0.02 °C. Following the waveguide, to filter out the pump light, an 810 ± 10 nm bandpass filter is used. The light beam is then focused on an intensified CCD (ICCD) camera (Hamamatsu Photonics, C5909-08) to observe the beam spatial profile. The spatial images are observed while the device temperature is being adjusted. The results are shown in Fig. 3(c). The emission angle changed from collinear to non-collinear as the device temperature decreased from 59.4 °C to 59.0 °C. When the temperature was further decreased to 58 °C, the spatial separation also increased.

4.1. Ultra-broadband photon-pair generation using chirped QPM slab waveguide

We observed the spectra of parametric fluorescence emitted from our slab waveguides using a spectrometer (Princeton, Acton SP2300) connected to single-mode fiber A or B, as shown

Optics EXPRESS

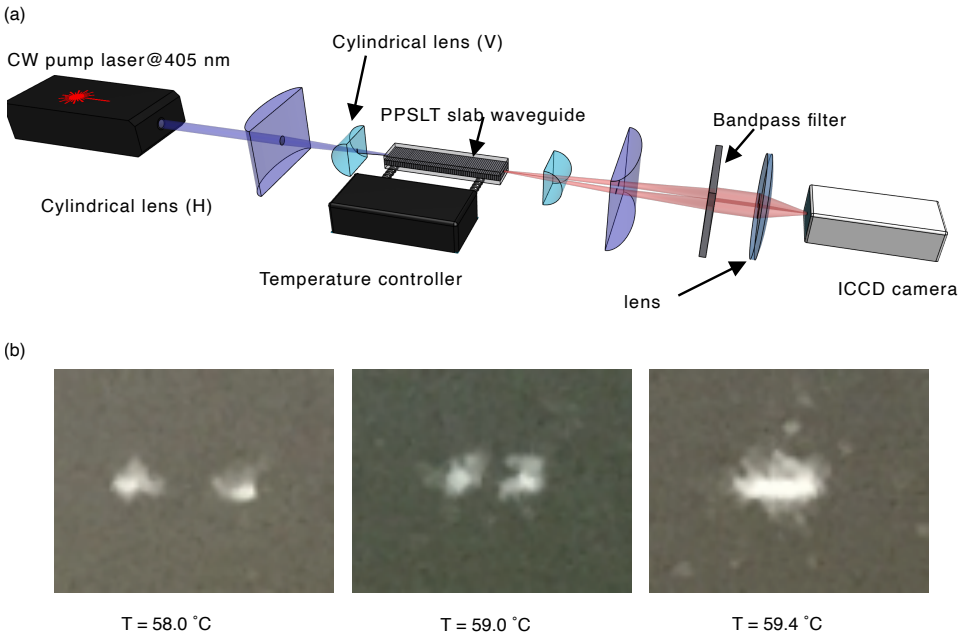

Fig. 3. (a) Experimental setup used to observe spatial profile of parametric fluorescence while tuning device temperature. (b) Intensified CCD (ICCD) camera images of SPDC light emitted using non-chirped slab waveguide while tuning the device temperature from 58.0 °C (non-collinear emission condition) to 59.4 °C (collinear emission condition).

in Fig. 4. In this experiment, 404.9 nm pump light (Coherent, MBR110, and MBD200) is condensed horizontally and vertically using a pair of cylindrical lenses, a 200 mm cylindrical lens (Newport, CKX200) for condensing the beam horizontally and a 3.9 mm cylindrical lens (Thorlabs, LJ1598L1-A) for condensing the beam vertically, and coupling the pump light into the waveguides. The typical pump light coupling efficiency (from air to waveguide) is about 20%. Then, the parametric fluorescence is collimated by another pair of cylindrical lenses with focal lengths of 3.9 mm (Thorlabs, LJ1598L1-B) and 80 mm (Thorlabs, LJ1105L2-B). A prism mirror is used to separate the non-collinearly emitted photon pairs into two independent optical paths. After eliminating the pump light with two longpass filters (Thorlabs, FELH0550), we couple the parametric downconverted photons into two single-mode fibers A and B (Thorlabs, P1-780PM-FC-2), then feed the photons to single-photon detectors or to the experimental setup shown in Fig. 7(a) for further measurements. In the following experiments, we set the device temperature to 57.5 °C with an accuracy of ± 0.02 °C.

For the non-chirped QPM waveguide, the measured spectra of signal and idler photons show single peaks at 810 nm with a bandwidth of 26 nm FWHM (Fig. 5(a)). The bandwidth for the measured spectra is larger than that for the simulation results. One possible reason for this could be the larger number of possible wave vectors involved in the SPDC process in the non-collinear condition.

We also observed expanded spectra of signal and idler photons when using a 3% chirped QPM slab waveguide. The FWHM bandwidth was 190 nm and the base-to-base width was 308 nm (682 to 990 nm). This results in Fig. 5(b) show an absence of frequency components at longer wavelengths, compared with the simulated results shown in Fig. 1(c), which may be due to chromatic aberration associated with the cylindrical lenses used to collimate the parametric

Optics EXPRESS

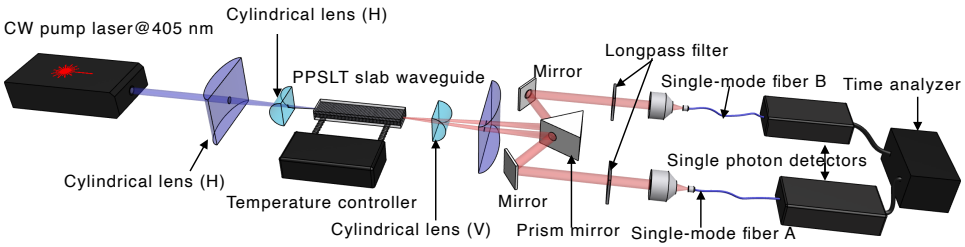

Fig. 4. Experimental setup for non-collinear emission of parametric fluorescence photon pairs. A 404.9 nm pump light is condensed by a pair of cylindrical lenses with focal lengths of 200 mm (horizontal direction) and 3.9 mm (vertical direction). The downconverted light beams are collimated by another pair of cylindrical lenses with focal lengths of 80 mm (horizontal direction) and 3.9 mm (vertical direction). A prism mirror is used to reflect the non-collinearly emitted photon pairs into two separate optical paths. A pair of longpass filters is used to eliminate the pump light. Photon pairs are coupled into two single-mode fibers A and B for detection. The device temperature is set to 57.5 °C.

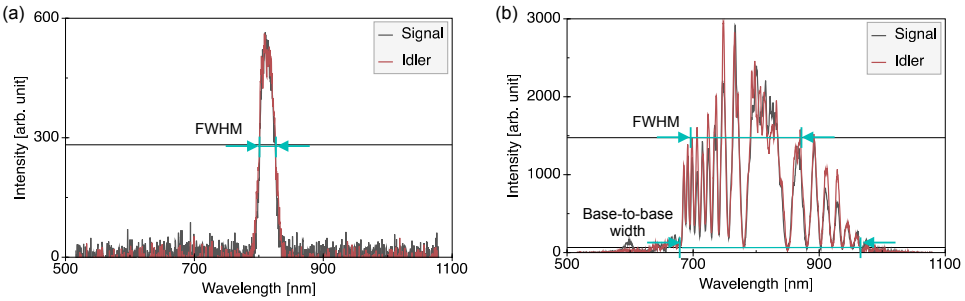

Fig. 5. (a) Measured parametric fluorescence photon pair spectra for non-chirped QPM slab waveguide. The FWHM is 26 nm. Signal and idler are photons emitted into different spatial modes. (b) Spectra measured with 3% chirped QPM slab waveguide. The FWHM bandwidth is 190 nm and the base-to-base width is 308 nm.

fluorescence light and the lens used for single-mode fiber coupling. In addition, the CCD camera in our spectrometer has a reduced quantum efficiency at long wavelengths. On the other hand, the unexpected frequency components with shorter wavelength could be explained by emission under the phase matching conditions of higher order guided modes. Similar to the simulated results, comb-like spectra are observed in the experimental results.

4.2. Highly efficient photon pair generation using slab waveguides

To evaluate the generation efficiency of our slab waveguides, we carried out photon pair correlation measurements. Photon pairs are generated and collected into single-mode fibers using the setup shown in Fig. 4. The photons are then fed into the detection unit where two single-photon counting modules (SPCMs) (Excilitas, AQHR-14-FC) are used for single-count event measurements. The coincidence count events are measured by a time analyzer (ID Quantique, id800) with a coincidence window width of 4 ns.

As shown in Figs. 6(a) and (b) for the non-chirped and 3% chirped slab waveguides, respectively, the measured single and coincidence count rates are proportional to the pump light power. Background counts and accidental coincidence counts are subtracted from these results. The total generation rate N_0 can be simply estimated as $N_0 = N_a \times N_b / N_{cc}$, where N_a and N_b are the single count rates obtained with detectors a and b, and N_{cc} is the coincidence count rate. The results of

Optics EXPRESS

linear fitting indicate that the single-count rates using the non-chirped slab waveguide are N_a = 1.6×10^5 counts/(μW·s) and N_b = 1.6×10^5 counts/(μW·s). The coincidence count rate N_{cc} is 1.1×10^4 counts/(μW·s). Therefore, the generation efficiency of our non-chirped slab waveguide is N_0 = 2.4×10^6 pairs/(μW·s). For the 3% chirped slab waveguide, the single and coincidence count rates are N_a = 4.0×10^4 counts/(μW·s), N_b = 3.7×10^4 counts/(μW·s), and N_{cc} = 1.8×10^3 counts/(μW·s). The generation efficiency of the 3% chirped device is 8.2×10^5 pairs/(μW·s). The coupling efficiency of photons from waveguide to single mode fibers can be simply estimated by $\eta_{cp} = 2\,N_{cc}/(\eta_{de}(N_a + N_b))$, where η_{de} is the detection efficiency, which is assumed to be 50%. In the case of using the non-chirped device, the η_{cp} = 13%, and while using a 3% chirped device, the η_{cp} = 9%. The primary culprit of loss is due to two factors. The first one is chromatic aberration in the lenses used to collect photons into single mode fibers. And the second is the difficulty in collecting photon pairs emitted from multiple segments with variable emission angles. Note that we believe that the propagation loss inside the PPSLT slab waveguide of both the pump light (405 nm) and the SPDC light (682nm to 990nm) are insignificant because the SLT crystal has a transparent range of 270 nm to 5500 nm and the waveguide core is 3 μm in size (height), which is much greater than the longest wavelength component of the generated SPDC photons.

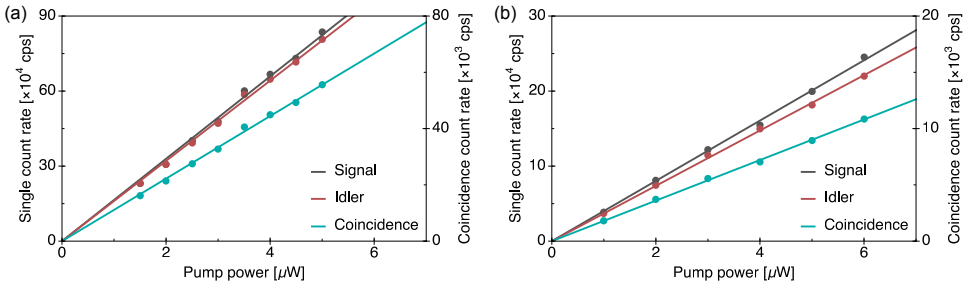

Fig. 6. (a) Single and coincidence counting events measured using non-chirped device. The black and red dots are the measured single-count events against pump light power, and the blue dots are the coincidence count events. The black, red, and blue lines are linear fits to the experiment data. (b) Single and coincidence counting events measured with a 3% chirped slab waveguide.

Table 1, compares these results to those for our previously reported QPM devices. The generation efficiency for our 20 mm long non-chirped slab waveguide under non-collinear emission conditions is comparable to that for a 10 mm non-chirped ridge waveguide device under collinear emission conditions [30]. However, the generation efficiency for the 3% chirped QPM slab waveguide is 70% less than that for a 3% chirped ridge waveguide. This reduction in efficiency may be caused by two reasons. One is the effect of interference of multiple phase matching functions with larger phase deviations in a longer device. The other reason is that slab waveguides have a lower pump power density than ridge waveguides, since slab waveguides only confine the pump light beam in one dimension. The generation efficiency for the chirped QPM slab waveguide is over 400 times higher than that for a 20 mm long 6.7% chirped QPM PPSLT bulk [11]. We believe that slab waveguides have advantages for both waveguide devices and bulk devices, namely, slab waveguides generate photon pairs with an efficiency close to that for ridge waveguides and can emit photon pairs into separate spatial modes like bulk crystals. This is critical for applications such as QOCT.

Optics EXPRESS

Table 1. Comparison of PPSLT chirped QPM devices.

Device	Chirp rate	Device length (mm)	Segments	Bandwidth FWHM (nm)	Generation efficiency (pairs/(μW·s))
Slab	0%	20	10	26	2.4×10^6
waveguide	3%	20	10	190	8.2×10^5
Ridge [30]	0%	10	10	16	2.7×10^6
waveguide	3%	10	10	229	2.7×10^6
Bulk [11]	6.7%	20	100	380	2.0×10^3

5. Two-photon interference measurements using slab waveguides

Slab waveguides can be directly used as parametric fluorescence sources for applications like QOCT without any post-selecting process. Therefore, we also carried out HOM measurements using the setup shown in Fig. 7(a). Non-collinearly emitted signal and idler photons are coupled into single-mode fibers A and B (in Fig. 4) and then connected to inputs 1 and 2 of the interferometer separately. Two pairs of quarter waveplates (QWPs) and polarization beamsplitters (PBSs) are used in the sample and reference arms as a pair of polarization circulators to improve the total transmission efficiency of the interferometer [16]. In the following HOM experiments, we placed a mirror in the sample arm as the measurement sample, and installed another mirror on a motorized stage to adjust the optical path length in the reference arm. After interference at the non-polarized beam splitter (BS), photons are coupled into single-mode fibers again at outputs 1 and 2, then sent to the detection unit (Fig. 7(b)) for coincidence measurements.

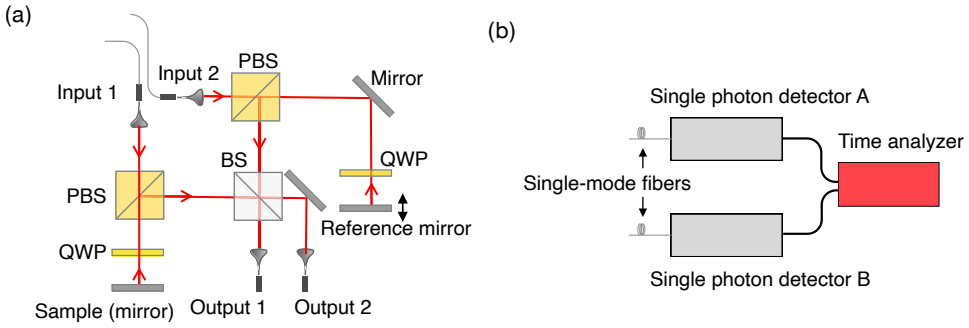

Fig. 7. (a) HOM measurement setup. We use quarter waveplates (QWPs) and polarization beamsplitters (PBSs) to improve the transmission efficiency of our interferometer. In the reference arm, a mirror mounted on a motorized stage is used for adjusting the optical path length. (b) Event-counting detection unit. Single photons are fed into detectors A and B using single-mode fibers. Single-count events are measured by two single-photon detectors, and coincidence events are recorded by a time analyzer.

In this experiment, we first pump the non-chirped QPM slab waveguide, using laser light (Coherent, MBD200) with a power of 50 mW and a wavelength of 404.9 nm. Then, non-collinearly emitted photon pairs are fed into a HOM interferometer as shown in Fig. 4(b) and photons are detected using two SPCMs. The coincidence count rates are recorded using a time analyzer (ID Quantique, id800) with a coincidence window width of 4 ns. As shown by the red dots in Fig. 8(a), we observed a HOM dip with a FWHM of 7.7±0.2 μm , estimated using Gaussian fitting. The black curve in the figure is the theoretical calculation result using the measured spectrum, which has a width of 7.2 μm and matches the experimental result. The HOM interference visibility $V = (N_{max} - N_{min})/N_{max}$ of this dip is 98% after subtracting accidental

Optics EXPRESS

counts, where N_{max} and N_{min} are the average base count rate and dip count rate for the HOM results.

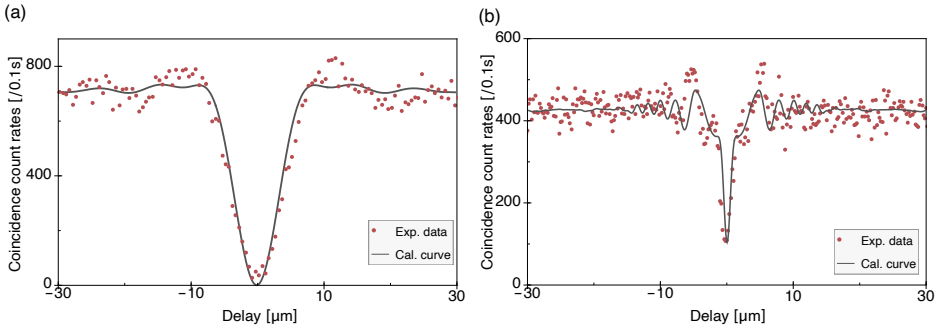

Fig. 8. HOM dips measured with slab waveguides after subtracting accidental coincidence counts. (a) HOM interference measured using non-chirped slab waveguide as photon pair source (red dots). The width of this HOM dip is 7.7±0.2 μm, and the visibility is 98%. The black curve is calculated using the measured spectra. (b) Results using 3% chirped device. The measured HOM dip width is 2±0.1 μm and the visibility is 74%.

In the experiment using the 3% chirped device, a superconducting single-photon detector (SSPDs) (Scontel, FCOPRS-CCR-SW60-LW60) and a SPCM are used as photon detectors. Coincidence counts are measured with a coincidence window of 1 ns using a time analyzer (ID Quantique, id900). We observed a HOM dip with a FWHM of 2.0±0.1 μm, as shown by the red dots in Fig. 8(b). In our theoretical calculations after considering the loss from single-mode fiber coupling, the FWHM of the HOM dip was 1.4 μm. This decrease in the HOM dip width may be caused by a lower detection efficiency when detecting photons with longer wavelengths. The visibility of this HOM dip after subtracting the accidental coincidence counts was 74%. The degradation in visibility measured with the 3% chirped device compared to that with the non-chirped device could be explained by optical system loss and the uneven splitting ratio of the 50:50 beamsplitter over the wide range of wavelengths used in the HOM interferometer.

6. Conclusion

Broadband photon pair sources using conversational QPM bulk crystals have insufficient brightness, whereas QPM ridge waveguide devices are highly efficient but only emit photon pairs in the same spatial mode. To develop an efficient photon pair source that can be directly used in applications based on two photon interference, we propose a chirped QPM PPSLT device that combines a chirped QPM and a slab waveguide structure. This device is developed for ultra-broadband and highly efficient generation of spatially separable parametric fluorescence photon pairs. In experiments, we observed a spectrum with a FWHM bandwidth of 26 nm using a non-chirped slab waveguide and a FWHM bandwidth of 190 nm (base-to-base width of 308 nm) using a 3% chirped QPM slab waveguide. Moreover, we observed a generation efficiency of 2.4×10^6 pairs/(μW·s) using the non-chirped device and 8×10^5 pairs/(μW·s) using the 3% chirped device under non-collinear emission conditions after single-mode fiber coupling. Additionally, we performed two-photon interference experiments using slab waveguides as photon sources and obtained a HOM dip with a FWHM of 7.7μm and a visibility of 98% using the non-chirped device. When using the 3% chirped device, the HOM measurement results show a dip with a FWHM of 2 μm and a visibility of 74%. We believe that, when employed as a photon pair source, slab waveguide QPM devices have the benefits of ridge waveguides (high brightness) and

Optics EXPRESS

bulk crystals (non-collinear emission capability), and are promising for a wide range of optical applications.

Funding. Core Research for Evolutional Science and Technology (Grant No. JPMJCR1674); Ministry of Education, Culture, Sports, Science and Technology, Quantum Leap Flagship Program (Grant No. JPMXS0118067634); Cabinet Office, Government of Japan PRISM; Japan Society for the Promotion of Science (Grant No. 21H04444); MEXT WISE Program.

Acknowledgments. We wish to thank Zhenghao Yin for help in the simulation of the effective refractive index.

Disclosures. The authors declare that there are no conflicts of interest related to this article.

Data availability. Data underlying the results presented in this paper are not publicly available at this time but may be obtained from the authors upon reasonable request.

References

1. H.-H. Lu, J. M. Lukens, N. A. Peters, B. P. Williams, A. M. Weiner, and P. Lougovski, "Quantum interference and correlation control of frequency-bin qubits," Optica **5**(11), 1455–1460 (2018).
2. L. Olislager, J. Cussey, A. T. Nguyen, P. Emplit, S. Massar, J.-M. Merolla, and K. P. Huy, "Frequency-bin entangled photons," Phys. Rev. A **82**(1), 013804 (2010).
3. B. Brecht, D. V. Reddy, C. Silberhorn, and M. G. Raymer, "Photon temporal modes: a complete framework for quantum information science," Phys. Rev. X **5**(4), 041017 (2015).
4. J. Nunn, L. Wright, C. Söller, L. Zhang, I. Walmsley, and B. Smith, "Large-alphabet time-frequency entangled quantum key distribution by means of time-to-frequency conversion," Opt. Express **21**(13), 15959–15973 (2013).
5. L. Sheridan and V. Scarani, "Security proof for quantum key distribution using qudit systems," Phys. Rev. A **82**(3), 030301 (2010).
6. A. Yabushita and T. Kobayashi, "Spectroscopy by frequency-entangled photon pairs," Phys. Rev. A **69**(1), 013806 (2004).
7. Y. Mukai, M. Arahata, T. Tashima, R. Okamoto, and S. Takeuchi, "Quantum Fourier-transform infrared spectroscopy for complex transmittance measurements," Phys. Rev. Appl. **15**(3), 034019 (2021).
8. D. A. Kalashnikov, A. V. Paterova, S. P. Kulik, and L. A. Krivitsky, "Infrared spectroscopy with visible light," Nat. Photonics **10**(2), 98–101 (2016).
9. Y. Mukai, R. Okamoto, and S. Takeuchi, "Quantum Fourier-transform infrared spectroscopy in the fingerprint region," Opt. Express **30**(13), 22624–22636 (2022).
10. M. Okano, R. Okamoto, A. Tanaka, S. Ishida, N. Nishizawa, and S. Takeuchi, "Dispersion cancellation in high-resolution two-photon interference," Phys. Rev. A **88**(4), 043845 (2013).
11. M. Okano, H. H. Lim, R. Okamoto, N. Nishizawa, S. Kurimura, and S. Takeuchi, "0.54 μm resolution two-photon interference with dispersion cancellation for quantum optical coherence tomography," Sci. Rep. **5**(1), 18042 (2015).
12. S. M. Kolenderska, F. Vanholsbeeck, and P. Kolenderski, "Fourier domain quantum optical coherence tomography," Opt. Express **28**(20), 29576–29589 (2020).
13. M. B. Nasr, B. E. Saleh, A. V. Sergienko, and M. C. Teich, "Demonstration of dispersion-canceled quantum-optical coherence tomography," Phys. Rev. Lett. **91**(8), 083601 (2003).
14. B. Dayan, A. Pe'Er, A. A. Friesem, and Y. Silberberg, "Two photon absorption and coherent control with broadband down-converted light," Phys. Rev. Lett. **93**(2), 023005 (2004).
15. H. Oka, "Enhanced vibrational-mode-selective two-step excitation using ultrabroadband frequency-entangled photons," Phys. Rev. A **97**(6), 063859 (2018).
16. K. Hayama, B. Cao, R. Okamoto, S. Suezawa, M. Okano, and S. Takeuchi, "High-depth-resolution imaging of dispersive samples using quantum optical coherence tomography," Opt. Lett. **47**(19), 4949–4952 (2022).
17. M. Okano, R. Okamoto, A. Tanaka, S. Subashchandran, and S. Takeuchi, "Generation of broadband spontaneous parametric fluorescence using multiple bulk nonlinear crystals," Opt. Express **20**(13), 13977–13987 (2012).
18. M. Hojo and K. Tanaka, "Broadband infrared light source by simultaneous parametric down-conversion," Sci. Rep. **11**(1), 17986 (2021).
19. Y. Shaked, R. Pomerantz, R. Z. Vered, and A. Pe'er, "Observing the nonclassical nature of ultra-broadband bi-photons at ultrafast speed," New J. Phys. **16**(5), 053012 (2014).
20. Y. Shaked, S. Yefet, T. Geller, and A. Pe'er, "Octave-spanning spectral phase control for single-cycle bi-photons," New J. Phys. **17**(7), 073024 (2015).
21. Y. Shaked, Y. Michael, R. Z. Vered, L. Bello, M. Rosenbluh, and A. Pe'er, "Lifting the bandwidth limit of optical homodyne measurement with broadband parametric amplification," Nat. Commun. **9**(1), 609 (2018).
22. M. Arahata, Y. Mukai, B. Cao, T. Tashima, R. Okamoto, and S. Takeuchi, "Wavelength variable generation and detection of photon pairs in visible and mid-infrared regions via spontaneous parametric downconversion," J. Opt. Soc. Am. B **38**(6), 1934–1941 (2021).
23. Z. Yin, K. Sugiura, H. Takashima, R. Okamoto, F. Qiu, S. Yokoyama, and S. Takeuchi, "Frequency correlated photon generation at telecom band using silicon nitride ring cavities," Opt. Express **29**(4), 4821–4829 (2021).
24. K. Sugiura, Z. Yin, R. Okamoto, L. Zhang, L. Kang, J. Chen, P. Wu, S. Chu, B. Little, and S. Takeuchi, "Broadband generation of photon-pairs from a cmos compatible device," Appl. Phys. Lett. **116**(22), 224001 (2020).

Optics EXPRESS

25. A. Tanaka, R. Okamoto, H. H. Lim, S. Subashchandran, M. Okano, L. Zhang, L. Kang, J. Chen, P. Wu, T. Hirohata, S. Kurimura, and S. Takeuchi, "Noncollinear parametric fluorescence by chirped quasi-phase matching for monocycle temporal entanglement," Opt. Express **20**(23), 25228–25238 (2012).
26. S. Carrasco, J. P. Torres, L. Torner, A. Sergienko, B. E. Saleh, and M. C. Teich, "Enhancing the axial resolution of quantum optical coherence tomography by chirped quasi-phase matching," Opt. Lett. **29**(20), 2429–2431 (2004).
27. S. Harris, "Chirp and compress: toward single-cycle biphotons," Phys. Rev. Lett. **98**(6), 063602 (2007).
28. M. B. Nasr, S. Carrasco, B. E. Saleh, A. V. Sergienko, M. C. Teich, J. P. Torres, L. Torner, D. S. Hum, and M. M. Fejer, "Ultrabroadband biphotons generated via chirped quasi-phase-matched optical parametric down-conversion," Phys. Rev. Lett. **100**(18), 183601 (2008).
29. S. Sensarn, G. Yin, and S. Harris, "Generation and compression of chirped biphotons," Phys. Rev. Lett. **104**(25), 253602 (2010).
30. B. Cao, M. Hisamitsu, K. Tokuda, S. Kurimura, R. Okamoto, and S. Takeuchi, "Efficient generation of ultra-broadband parametric fluorescence using chirped quasi-phase-matched waveguide devices," Opt. Express **29**(14), 21615–21628 (2021).
31. A. Burlakov, M. Chekhova, O. Karabutova, and S. Kulik, "Collinear two-photon state with spectral properties of type-i and polarization properties of type-ii spontaneous parametric down-conversion: Preparation and testing," Phys. Rev. A **64**(4), 041803 (2001).
32. Y. Kamei, C. Bo, R. Okamoto, and S. Takeuchi, "Spatial separation of collinearly emitted broadband frequency-correlated photon pairs," Phys. Rev. A **107**(1), L010601 (2023).
33. A. Dosseva, Ł. Cincio, and A. M. Brańczyk, "Shaping the joint spectrum of down-converted photons through optimized custom poling," Phys. Rev. A **93**(1), 013801 (2016).
34. A. Bruner, D. Eger, M. B. Oron, P. Blau, M. Katz, and S. Ruschin, "Temperature-dependent sellmeier equation for the refractive index of stoichiometric lithium tantalate," Opt. Lett. **28**(3), 194–196 (2003).